High Power Laser Science and Engineering, (2018), Vol. 6, e31, 8 pages.

doi:10.1017/hpl.2018.25

Measurement and analysis of K-shell lines of silicon ions in laser plasmas

Bo Han[1], Feilu Wang[2], Jiayong Zhong[1,5], Guiyun Liang[2], Huigang Wei[2], Dawei Yuan[2], Baojun Zhu[3], Fang Li[3], Chang Liu[1], Yanfei Li[3], Jiarui Zhao[3], Zhe Zhang[3], Chen Wang[6], Jun Xiong[6], Guo Jia[6], Neng Hua[7], Jianqiang Zhu[7], Yutong Li[3,5], Gang Zhao[2], and Jie Zhang[4,5]

[1]*Department of Astronomy, Beijing Normal University, Beijing 100875, China*

[2]*Key Laboratory of Optical Astronomy, National Astronomical Observatories, Chinese Academy of Sciences, Beijing 100012, China*

[3]*National Laboratory for Condensed Matter Physics, Institute of Physics, Chinese Academy of Sciences, Beijing 100190, China*

[4]*Key Laboratory for Laser Plasmas (MoE) and Department of Physics and Astronomy, Shanghai Jiao Tong University, Shanghai 200240, China*

[5]*IFSA Collaborative Innovation Center, Shanghai Jiao Tong University, Shanghai 200240, China*

[6]*Research Center for Laser Fusion, China Academy of Engineering Physics, Mianyang 621900, China*

[7]*National Laboratory on High Power Laser and Physics, Chinese Academy of Sciences, Shanghai 201800, China*

(Received 29 November 2017; revised 23 February 2018; accepted 29 March 2018)

Abstract

We present laboratory measurement and theoretical analysis of silicon K-shell lines in plasmas produced by Shenguang II laser facility, and discuss the application of line ratios to diagnose the electron density and temperature of laser plasmas. Two types of shots were carried out to interpret silicon plasma spectra under two conditions, and the spectra from 6.6 Å to 6.85 Å were measured. The radiative-collisional code based on the flexible atomic code (RCF) is used to identify the lines, and it also well simulates the experimental spectra. Satellite lines, which are populated by dielectron capture and large radiative decay rate, influence the spectrum profile significantly. Because of the blending of lines, the traditional G value and R value are not applicable in diagnosing electron temperature and density of plasma. We take the contribution of satellite lines into the calculation of line ratios of He-α lines, and discuss their relations with the electron temperature and density.

Keywords: high energy density physics; laser plasmas interaction; plasmas astrophysics

1. Introduction

K-shell lines of elements from astrophysical X-ray sources have been widely identified in high-resolution spectra, which are observed by X-ray satellites, such as Chandra and XMM-Newton. There are not only strong emission lines from photoionized plasmas of X-ray binaries[1–3], but also absorption lines from active galactic nuclei (AGNs)[4, 5]. The lines of He-like ions are signs of presence of highly ionized plasmas, and they are useful to diagnose experimental and astrophysical plasma properties, such as electron density and temperature[1, 3, 6–8]. Therefore, modeling and analyzing these high-resolution spectra, accurate atomic data and spectroscopy interpretation for the K-shell lines are urgently needed.

Many theoretical calculations[4, 9–11] have been performed to derive the wavelengths and transition rates of K-shell lines using kinds of atom structure codes. These include using HFR[12] and AUTOSTRUCTURE[13, 14] to calculate the wavelength and A-values of K-shell lines for some medium-Z elements. Their results agree well with the other previous works[4, 9], but some disagreements still exist, for example, the difference from C-like ions radiative rates can be 40%[9, 11, 15]. In order to benchmark and testify the theoretical results, some experiments were carried out to measure the wavelengths of K-shell lines. Refs. [16, 17] measured and identified K-shell lines in X-ray spectrum of foil-excited silicon. These lines were proved to be emitted by K-shell transitions in Si VIII–XIII, as well as by two electron

Correspondence to: J. Zhong, Department of Astronomy, Beijing Normal University, No. 19 Xinjiekouwai St, Haidian District, Beijing 100875, China. Email: jyzhong@bnu.edu.cn

one photon transitions. Ref. [18] reported $2p \rightarrow 1s$ transition lines in Si XI to Si XIV ions in beam-foil experiment. Ref. [19] measured satellites lines of Be-like through F-like ions for $Z = 12$–16 elements in laser plasmas produced by a CO_2-laser. Ref. [20] measured Kα transitions of silicon ions using EBIT-I electron beam ion trap at the Lawrence Livermore National Laboratory.

Few of the former works interpreted the line emission mechanism in detail. More importantly, we find that satellite lines may be blended with the He-like triplet lines, and impact their line ratios, which are widely used in plasma diagnosis. Here, we report the spectroscopic experiment of silicon on Shenguang II laser facility and the recalculated line ratios of He-like triplet. Section 2 is the experimental setups and calibrated spectra. Theoretical simulations and discussions about line emission mechanism are presented in Section 3. Section 4 presents the influence of satellite lines on the line ratios of He-like triplet, and the application to diagnose electron density and temperature is also discussed. Conclusion is in Section 5.

2. Experimental setups and spectra

The experiments were carried out on the Shenguang II laser facility at Shanghai Institute of Optics and Fine Mechanics, Chinese Academy of Sciences. Two types of targets were performed to get the spectra of highly charged silicon ions. Figure 1(a) shows the Type I target, and the main part is a silicon plate with 400 μm in diameter. Shot 24 and Shot 26 used the Type I target. Figure 1(b) shows the Type II target and the schematic diagram of the experimental setups. In Type II target, a CH foil perpendicular to the silicon plate was added to the Type I target, which was used to obstruct the plasma evolution. Shot 28 and Shot 32 used the Type II target. In both types of shots, the center of the silicon plate lower surface was set at the target chamber center (TCC), and two 240 J driven laser beams were used, whose wavelengths were 351 nm and durations were 1 ns. The diameters of the focal spots were about 150 μm full-width at half-maximum (FWHM), and the incident laser intensity is about 2.4×10^{15} W · cm^{-2}[21]. A crystal spectrometer[22] was used to record the spectrum of plasma. Additionally, another laser, whose wavelength was 527 nm and duration was 30 ps, was used as a probe. The profile of the plasmas was measured by a Nomarski interferometer, whose magnification factor was three[21]. Both types of shots were repeated twice, and the repeatability is quite good. The experimental spectra are shown in Figures 2 and 3. However, the Type II spectra were impacted by some Cu lines, which were from the copper frame of the CH foil. We repeated the Type II target in 2017 with the beam energy raised to 250 J. The repeated Type II spectrum is shown in Figure 4. The slight differences in spectral intensities between the two shots of each type may result from laser energy deviation.

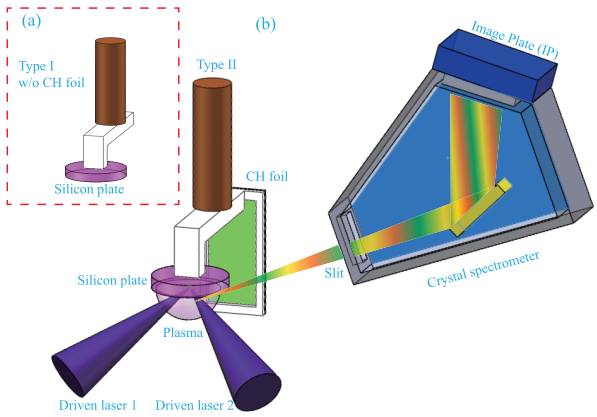

Figure 1. Two types of targets and schematic diagram of the experimental setups. (a) The Type I target. (b) The Type II shot and the schematic diagram of the experimental setups. The silicon plate is set at the target chamber center (TCC), and two driven laser beams are focused on it. A crystal spectrometer is used to record the spectrum of plasma.

Figures 5(a) and 5(b) are the interferograms of Type I and Type II shots with the probe beam delayed for 3 ns. This is obvious that the plasma of Type II shot has more complex construction than that of Type I shot. In other words, the CH foil impacted the evolution of the plasmas. Moreover, by Abel inversing the interferograms, the electron density distributions of the plasmas can be deduced, which are shown in Figures 2(c) and 2(d). The electron densities of the plasmas are generally above 10^{18} cm^{-3}.

3. Theoretical simulations

We use the radiative-collisional code (RCF) based on flexible atomic code (FAC)[23] to simulate the experimental spectra. RCF is a code for steady-state plasmas, which is under nonlocal thermodynamic equilibrium condition. All the atomic data are calculated by the FAC[24] , which ensures calculating completeness and consistency of atomic data. Applied to some photoionization experiments, RCF well reproduces the charge state distribution of photoionizing Fe experiment, which was carried out by Foord *et al.* on Z-facility[23, 25, 26], and the emission spectrum of photoionizing Si experiment, which was achieved by Fujioka *et al.* on GEKKO-XII[27, 28].

The atomic data include ions from C-like to bare nuclei. The maximum of principle quantum number, $n_{\max}$, is limited to 4 for C-like, B-like and Be-like ions. $n_{\max}$s of Li-like, He-like and H-like ions are 7. In the simulations, the plasmas are assumed to be in collisional radiative steady state. Collisional processes include collisional excitation, collisional ionization, autoionization and their inverse processes, which are collisional deexcitation, three-body recombination and dielectron capture. Radiative processes include radiative recombination and E1, E2, M1 and M2 types of radiative

https://doi.org/10.1017/hpl.2018.25 Published online by Cambridge University Press

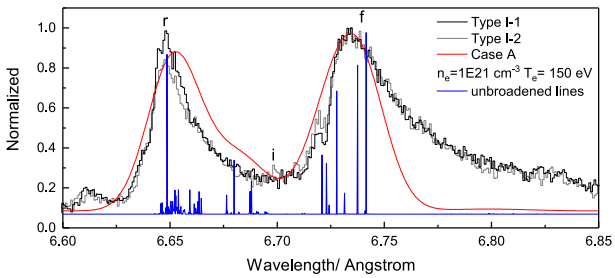

Figure 2. Black and gray lines are the experimental spectra of two Type I shots. Red line is the simulation results (Case A), where $n_e = 10^{21}$ cm^{-3} and $T_e = 150$ eV. Blue line is the unbroadened theoretical line.

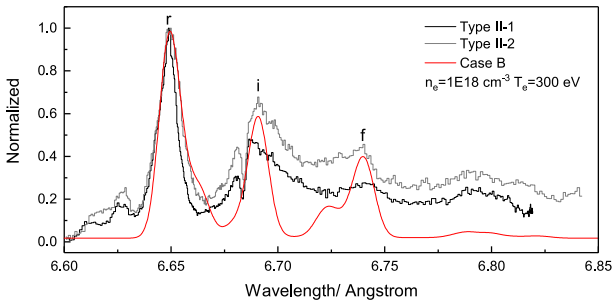

Figure 3. Black and gray lines are the experimental spectra of two Type II shots. Red line is the simulation results (Case B), where $n_e = 10^{18}$ cm^{-3} and $T_e = 300$ eV.

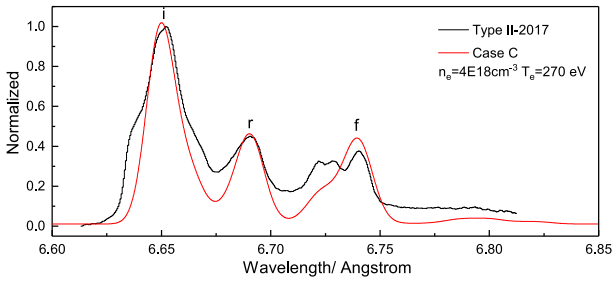

Figure 4. Black line is the experimental spectrum of repeated Type II targets in 2017. Red line is the simulation results (Case C), where $n_e = 5 \times 10^{18}$ cm^{-3} and $T_e = 250$ eV.

decays. The spectra we are interested in, are from the He-like and Li-like ions, which only exist in highly ionized plasma. Although the spectra might be influenced by lines from lower ionized ions, the comparison between the experimental and theoretical spectra shows that the influence is small, such as the tail of the second peaks in Figure 2. So we assume the plasmas are in steady state, which are highly ionized. In all the following RCF theoretical spectra, line intensities are convolved using Gaussian profile with an FWHM about 5 m Å (1 eV in energy).

Figures 2–4 show the simulation results. Case A, where the electron density is 10^{21} cm^{-3} and the electron temperature is 150 eV, well reproduces the two stocky peaks in the Type I spectra. The tail of the second peak in long wavelength range may attribute to the lines of Be-like and B-like ions, which are emitted in low temperature condition. In Case B, most of the peaks in Type II spectrum are reproduced, and the input parameters are $n_e = 10^{18}$ cm^{-3} and $T_e = 300$ eV. The unproduced peaks may be Cu L-shell lines, which are emitted by the copper frame of the CH foil[29]. Figure 4 shows the Si spectrum without Cu lines, and Case C gets a better result than Case B. The big differences of the two groups of input parameters indicate that the CH foil impacted the evolution of the plasma in Type II shots. It seems that the low density and high temperature part of plasma expanded and dissipated quickly in the Type I shot. Then, the spectrum of the high density but low temperature part was recorded. While in the Type II shots, the low density part was reflected by the CH foil, diluting the high density part. The accurate evolution needs hydrodynamic simulation, but we only talk about the spectrum emission in the present paper. The intense lines in these two cases are listed in Tables 1 and 2. In addition, the available wavelength results of Palmeri *et al.*[9] are also listed in Tables 1 and 2 as comparison. Two groups of data are in good agreement, and the difference of most of the lines is less than 0.01 Å.

In Case A, each of the two stocky peaks is not formed by single transition, but forest of lines, as shown by the theoretical unbroadened lines in Figure 3. As Figure 3 and Table 1 show, the resonance line (r or $w/1s^2\,{}^1S_0$–$1s2p\,{}^1P_1$, 6.648 Å) contributes most of the intensity of the left peak. The rest part of the two peaks are constructed by transitions from $1s2l2l'$ to $1s^22l$, from $1s2l3l'$ to $1s^23l'$ and even from $1s2l4l'$ to $1s^24l'$. Because these lines are surrounded with the He-α lines, they are called satellite lines of the He-α lines. These lines not only huddle together, but also have similar intensities. Even though they are only convolved with an FWHM of 5 m Å, they are indistinguishable. As a result, two stocky peaks are formed, and the Gaussian centroids of the peaks shift a little from the strongest lines. In other words, the satellite lines blend with the He-like lines and affect the line strengths significantly. In Case B, there are also many Li-like lines, but the number of intense lines decreases and their relative intensities are large, so that the peaks become slightly thinner and more distinguishable than Case A.

In the two cases, the He-like ion has a fraction of 96% and 87%, respectively. The energy gaps between the $1s2l$ levels and ground state are larger than 1800 eV. While the electron temperature is several hundreds of eV in the two cases, most of the He-like ions are frozen at the ground state. The fraction of Li-like ion and H-like ion is much smaller than that of He-like ion, so that neither ionization nor recombination processes can populate the resonance line efficiently. Thus, the resonance line is mainly populated by collisional excitation from the tremendous amount of the ground state of He-like ion. Combing with large radiative decay rate, which is 3.87×10^{13} s^{-1}, the resonance line is the strongest line.

Under such conditions, where temperatures are hundreds of eV, the Li-like ion is easier to be ionized than to be excited

https://doi.org/10.1017/hpl.2018.25 Published online by Cambridge University Press

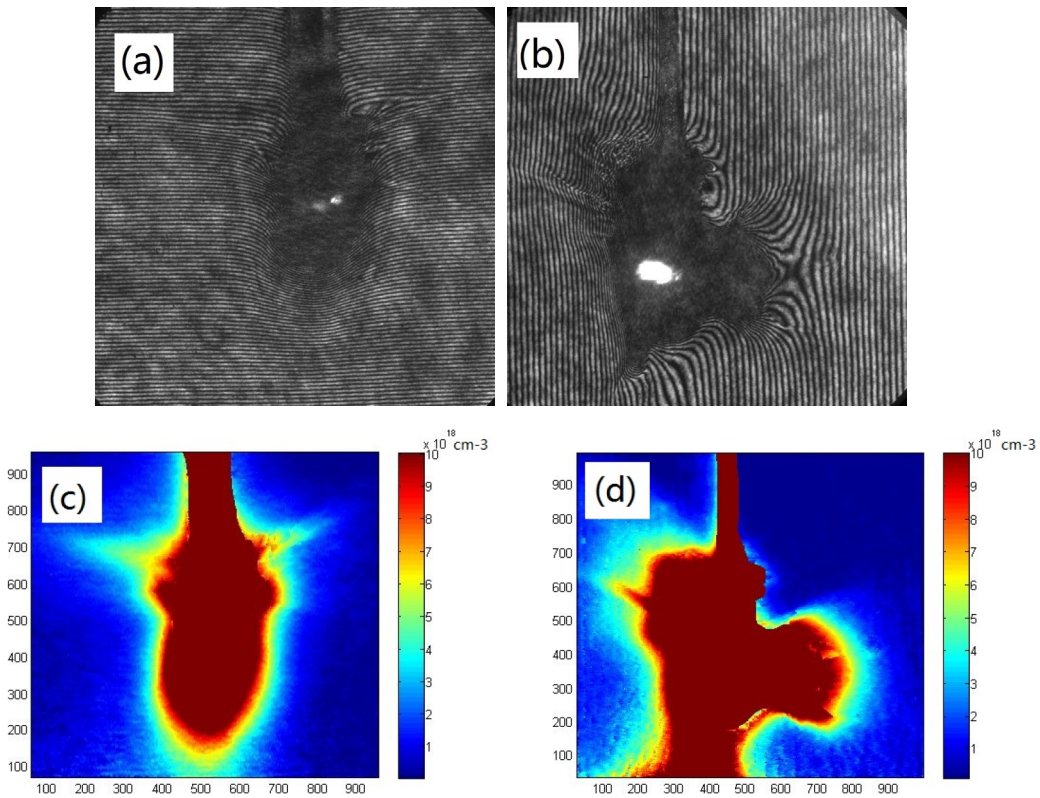

Figure 5. (a) and (b) are the interferograms of Type I and Type II shots. (c) and (d) are the electron density distribution deduced by Abel inversing of (a) and (b).

by collision, so that the Li-like ion has small populations. However, Li-like lines strongly affect the spectrum profile in the two cases. The reason is that these Li-like lines are populated by dielectronic capture from the ground state of He-like ion, and they also have comparable radiative decay rates with the resonance line. There are two main processes to produce Li-like ions with K-shell vacancies in a collision-dominating plasma, i.e., collisional excitation and dielectronic capture. Because of the small population of Li-like ion, the contribution of collisional excitation is negligible. The Li-like levels, which have K-shell vacancies, usually have large autoionization rates to the ground state of He-like ion. Therefore, dielectron capture, which is the reverse process of autoionization, has large reaction rate while the ground state of He-like ion has tremendous amount. Moreover, the doubly excited Li-like lines usually have comparable radiative decay rates with the resonance line. For example, the radiative decay rate of $1s^2 2s\ ^2S_{1/2}$ to $1s2s2p\ ^2P_{1/2}$ is 3.26×10^{13} s^{-1}. As a result, forest of intense Li-like lines are produced.

However, comparing with those above lines, the intercombination line (i or $x/1s^2\ ^1S_0$–$1s2p\ ^3P_2$ and $y/1s^2\ ^1S_0$–$1s2p\ ^3P_1$, 6.688 Å) and the forbidden line (f or $z/1s^2\ ^1S_0$–$1s2s\ ^3S_1$, 6.74 Å) are weaker. The reason is that the radiative decay rates of these two lines are too small. The A-value of intercombination is 1.36×10^{11} s^{-1} and 3.27×10^5 s^{-1} for the forbidden lines, which are several orders of magnitude smaller than those intense lines. When there are no other processes to make up this huge disadvantage, the intercombination and forbidden lines are drawn in the Li-like lines.

4. Developed G value and R value

The line G value ($G = (f + i)/r$) and R value ($R = f/i$) of He-α lines are widely used in experimental and astrophysical plasma diagnosis[6–8]. Some previous works[30–32] also reported that in some low-resolution spectra the satellite lines blend with the He-like lines, which is consistent with the present results. We have discussed the influence of satellite lines on these line ratios for photoionized plasmas, and they impact the diagnosing result significantly[33]. In this section, combining with the present experimental results, we discuss the influences of satellite lines on these two line ratios for the collision-dominating plasmas.

In the present experimental spectra, the intercombination and forbidden lines are weaker than the Li-like lines, and their positions are occupied by many Li-like lines. It is hard to distinguish these lines clearly and to measure their strengths accurately, and calculations of the line ratios are impossible. So we develop the identification of the G value and R value, where the contributions of the blending satellite

https://doi.org/10.1017/hpl.2018.25 Published online by Cambridge University Press

Table 1. Experimental peak centroids with statistical errors of Shot 26, and the present and theoretical wavelength of intense lines in Case A.

λ_{Exp} (Å)	Ion	$\lambda_{Pres.}$ (Å)	$\lambda_{Palmeri.}$ (Å)	Transition				Case
				Upper		Lower		
	Li	6.6457		$1s2p3d$	$^2P_{3/2}$	$1s^23d$	$^2D_{5/2}$	A
	Li	6.6462		$1s2p3d$	$^2P_{1/2}$	$1s^23d$	$^2D_{3/2}$	A
	Li	6.6479		$1s2p(1P)3p$	$^2S_{1/2}$	$1s^23p$	$^2P_{1/2}$	A
	He	6.6486	6.648	$1s2p$	$^1P_1$	$1s^2$	$^1S_0$	A
	Li	6.6491		$1s2p(1P)4f$	$^2D_{3/2}$	$1s^24d$	$^2D_{3/2}$	A
	Li	6.6491		$1s2p(1P)4f$	$^2D_{5/2}$	$1s^24d$	$^2D_{5/2}$	A
	Li	6.6503		$1s2p(1P)4f$	$^2G_{7/2}$	$1s^24d$	$^2D_{3/2}$	A
	Li	6.6504		$1s2p(1P)4f$	$^2G_{9/2}$	$1s^24d$	$^2D_{5/2}$	A
	Li	6.6506		$1s2p(1P)4d$	$^2P_{1/2}$	$1s^24f$	$^2F_{5/2}$	A
	Li	6.6523		$1s2p(1P)3d$	$^2F_{5/2}$	$1s^23d$	$^2D_{3/2}$	A
	Li	6.6527		$1s2p(1P)4f$	$^2F_{7/2}$	$1s^24d$	$^2D_{5/2}$	A
	Li	6.6527		$1s2p(1P)4f$	$^2F_{5/2}$	$1s^24d$	$^2D_{3/2}$	A
	Li	6.6539		$1s2p(1P)3d$	$^2F_{7/2}$	$1s^23d$	$^2D_{5/2}$	A
	Li	6.6544		$1s2p(1P)4d$	$^2F_{7/2}$	$1s^24f$	$^2F_{7/2}$	A
	Li	6.6549		$1s2p(1P)4d$	$^2D_{3/2}$	$1s^24f$	$^2F_{5/2}$	A
	Li	6.6551		$1s2p(1P)4s$	$^2P_{3/2}$	$1s^24s$	$^2S_{1/2}$	A
	Li	6.6552		$1s2p(1P)4s$	$^2P_{1/2}$	$1s^24s$	$^2S_{1/2}$	A
	Li	6.6562		$1s2p(1P)4p$	$^2P_{3/2}$	$1s^24p$	$^2P_{3/2}$	A
6.6565±0.0001	Li	6.6565		$1s2p(1P)4p$	$^2D_{5/2}$	$1s^24p$	$^2P_{1/2}$	A
	Li	6.6568		$1s2p(1P)4p$	$^2D_{3/2}$	$1s^24p$	$^2P_{3/2}$	A
	Li	6.6592		$1s2p(1P)3d$	$^2D_{5/2}$	$1s^23d$	$^2D_{5/2}$	A
	Li	6.6593		$1s2p(1P)3d$	$^2D_{3/2}$	$1s^23d$	$^2D_{3/2}$	A
	Li	6.6612		$1s2p(1P)3s$	$^2P_{1/2}$	$1s^23s$	$^2S_{1/2}$	A
	Li	6.6618		$1s2p(1P)3s$	$^2P_{3/2}$	$1s^23s$	$^2S_{1/2}$	A
	Li	6.6622		$1s2p(3P)3s$	$^2P_{3/2}$	$1s^23s$	$^2S_{1/2}$	A
	Li	6.663		$1s2p(1P)3p$	$^2P_{3/2}$	$1s^23s$	$^2P_{3/2}$	A
	Li	6.6635		$1s2p(1P)3p$	$^2D_{3/2}$	$1s^23s$	$^2P_{1/2}$	A
	Li	6.6635		$1s2p(1P)3p$	$^2P_{1/2}$	$1s^23s$	$^2P_{1/2}$	A
	Li	6.6646		$1s2p(1P)3p$	$^2D_{5/2}$	$1s^23s$	$^2P_{3/2}$	A
	Li	6.6764		$1s(2S)2p^2$	$^2S_{1/2}$	$1s^22p$	$^2P_{1/2}$	A
	Li	6.6799	6.6776	$1s(2S)2p^2$	$^2S_{1/2}$	$1s^2sp$	$^2P_{3/2}$	A
	Li	6.6872	6.6854	$1s(2S)2s2p(1Po)$	$^2P^o{}_{3/2}$	$1s^22s$	$^2S_{1/2}$	A
	Li	6.6878	6.6866	$1s(2S)2s2p(1Po)$	$^2P^o{}_{1/2}$	$1s^22s$	$^2S_{1/2}$	A
	Li	6.7207	6.7176	$1s(2S)2s2p(3Po)$	$^2P^o{}_{3/2}$	$1s^22s$	$^2S_{1/2}$	A
	Li	6.7228	6.7196	$1s(2S)2s2p(3Po)$	$^2P^o{}_{1/2}$	$1s^22s$	$^2S_{1/2}$	A
	Li	6.7242		$1s(2S)2p^2(3P)$	$^2P_{1/2}$	$1s^22p$	$^2P_{1/2}$	A
	Li	6.7277		$1s(2S)2p^2(1D)$	$^2D_{5/2}$	$1s^22p$	$^2P_{3/2}$	A
	Li	6.7278	6.7293	$1s(2S)2p^2(3P)$	$^2P_{1/2}$	$1s^22p$	$^2P_{3/2}$	A
6.7333±0.0001	Li	6.7374	6.7365	$1s(2S)2p^2(1D)$	$^2D_{5/2}$	$1s^22p$	$^2P_{1/2}$	A
	Li	6.7415	6.7398	$1s(2S)2p^2(1D)$	$^2D_{3/2}$	$1s^22p$	$^2P_{3/2}$	A

lines are taken into the line intensities. For simplicity, one can think that the three peaks in Figure 4 are the extended resonance, intercombination and forbidden lines, respectively. The developed line ratios are called as $G+$ value and $R+$ value[33]. The trends of G and $G+$ along with electron temperature are plotted in Figure 6, and the trends of R and $R+$ along with electron density are plotted in Figure 7. If the plasma is lowly ionized, there will be no intense Li-like and He-like lines, and the discussions about these two ratios are meaningless. The plotted line ratios are calculated in cases with average ionizations larger than 10.

As mentioned above, the intercombination and forbidden lines are much weaker than the resonance line, so that the G value is always very small. In Figure 6, the G value is insensitive to electron temperature. The reason is that the energy gap between the resonance line and the forbidden line is about 25 eV, but the temperature in calculation is hundreds of eV. Therefore, the G value is not obviously influenced by the temperature in this range. The changing of the input parameter is along with changing of ionization degree. When temperature rises, the fraction of Li-like ion decreases and He-like ion increases. The intensities of the lines change

https://doi.org/10.1017/hpl.2018.25 Published online by Cambridge University Press

Table 2. Experimental peak centroids with statistical errors from 6.6 Å to 6.85 Å of Shot 32 and the present and theoretical wavelength of intense lines in Case B.

λ_{Exp} (Å)	Ion	$\lambda_{Pres.}$ (Å)	$\lambda_{Palmeri.}$ (Å)	Transition				Case
				Upper		Lower		
6.627±0.0006								
6.648 ±0.0002	He	6.6486	6.648	$1s2p$	$^1P_1$	$1s^2$	$^1S_0$	B
	Li	6.6523		$1s2p(1P)3d$	$^2F_{5/2}$	$1s^23d$	$^2D_{3/2}$	B
	Li	6.6539		$1s2p(1P)3d$	$^2F_{7/2}$	$1s^23d$	$^2D_{5/2}$	B
	Li	6.6592		$1s2p(1P)3d$	$^2D_{5/2}$	$1s^23d$	$^2D_{5/2}$	B
	Li	6.6593		$1s2p(1P)3d$	$^2D_{3/2}$	$1s^23d$	$^2D_{3/2}$	B
	Li	6.6612		$1s2p(1P)3s$	$^2P_{1/2}$	$1s^23s$	$^2S_{1/2}$	B
	Li	6.6618		$1s2p(1P)3s$	$^2P_{3/2}$	$1s^23s$	$^2S_{1/2}$	B
	Li	6.663		$1s2p(1P)3p$	$^2P_{3/2}$	$1s^23s$	$^2P_{3/2}$	B
	Li	6.6635		$1s2p(1P)3p$	$^2D_{3/2}$	$1s^23s$	$^2P_{1/2}$	B
	Li	6.6635		$1s2p(1P)3p$	$^2P_{1/2}$	$1s^23s$	$^2P_{1/2}$	B
	Li	6.6646		$1s2p(1P)3p$	$^2D_{5/2}$	$1s^23s$	$^2P_{3/2}$	B
6.6829±0.0003	Li	6.6799	6.6776	$1s(2S)2p^2$	$^2S_{1/2}$	$1s^2sp$	$^2P_{3/2}$	B
	Li	6.6872	6.6854	$1s(2S)2s2p(1P)$	$^2P_{3/2}$	$1s^22s$	$^2S_{1/2}$	B
	Li	6.6878	6.6866	$1s(2S)2s2p(1P)$	$^2P_{1/2}$	$1s^22s$	$^2S_{1/2}$	B
6.688 ±0.0003	He	6.6911	6.6899	$1s2p$	$^3P_1$	$1s^2$	$^1S_0$	B
	Li	6.7207	6.7176	$1s(2S)2s2p(3P)$	$^2P_{3/2}$	$1s^22s$	$^2S_{1/2}$	B
6.7136±0.0005	Li	6.7228	6.7196	$1s(2S)2s2p(3P)$	$^2P_{1/2}$	$1s^22s$	$^2S_{1/2}$	B
	Li	6.7278	6.7293	$1s(2S)2p^2(3P)$	$^2P_{1/2}$	$1s^22p$	$^2P_{3/2}$	B
6.7372±0.0006	Li	6.7374	6.7365	$1s(2S)2p^2(1D)$	$^2D_{5/2}$	$1s^22p$	$^2P_{1/2}$	B
	Li	6.7415	6.7398	$1s(2S)2p^2(1D)$	$^2D_{3/2}$	$1s^22p$	$^2P_{3/2}$	B
	Be	6.7971	6.7992	$1s(2S)2s2p^2(4P)$	$^3P_1$	$1s^22s2p$	$^3P_1$	B
6.7952±0.0003	Be	6.7987	6.7995	$1s(2S)2s2p^2(4P)$	$^3P_2$	$1s^22p^2$	$^3P_2$	B
	Be	6.7989	6.8008	$1s(2S)2s2p^2(2D)$	$^3D_2$	$1s^22s2p$	$^3P_1$	B
	Be	6.7991	6.7999	$1s(2S)2s2p^2(2D)$	$^3D_1$	$1s^22s2p$	$^3P_0$	B
	Be	6.7995	6.8016	$1s(2S)2s2p^2(4P)$	$^3P_1$	$1s^22p^2$	$^3P_2$	B
	Be	6.8211	6.8046	$1s2p^3$	$^3D_3$	$1s^22p^2$	$^3P_2$	B
	Be	6.8251	6.8239	$1s(2S)2s2p^2(2P)$	$^3P_0$	$1s^22s2p$	$^1P_1$	B
	Be	6.8254	6.8249	$1s2p^3$	$^1P_1$	$1s^22p^2$	$^1S_0$	B

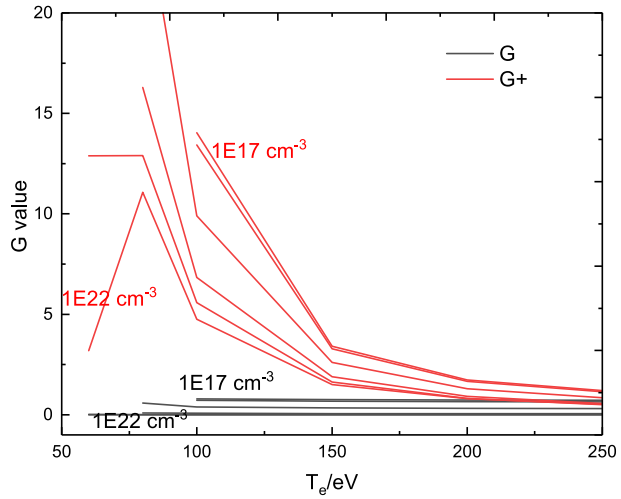

Figure 6. The $G+$ and G values. Every line has same electron density, which spans from 10^{17} cm^{-3} to 10^{22} cm^{-3} exponentially, and the line ratios are plotted as a function of electron temperature.

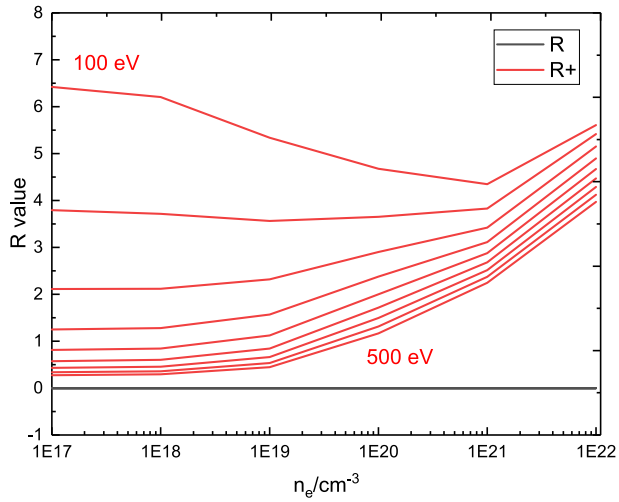

Figure 7. The $R+$ (red) and R (black) values. Every line has same electron temperature, which spans from 100 eV to 500 eV incrementally, and the line ratios are plotted as a function of electron density.

https://doi.org/10.1017/hpl.2018.25 Published online by Cambridge University Press

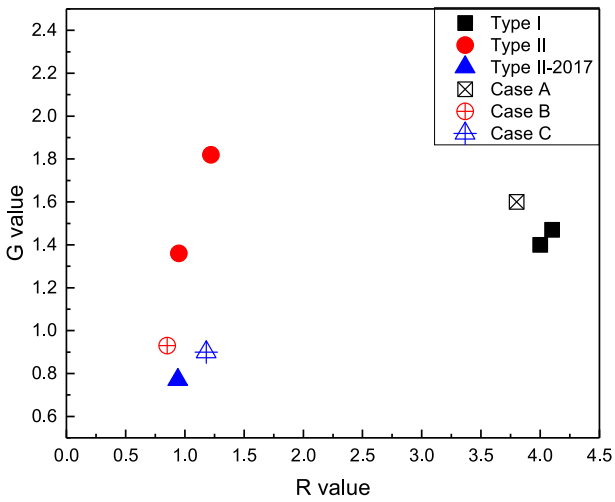

Figure 8. The solid scatters are the experimental R and G values. The open scatters are the $R+$ and $G+$ values of the three theoretical cases.

with the ions. We also know that the satellite lines enter the peaks a lot, which are at the position of the intercombination and forbidden lines. In consequence, $G+$ is quite large in the low temperature range, and decreases as the temperature rises. With same temperature, the low density case has lower ionization degree than the higher one. Thus, the $G+$ value of the lower density case is larger than that of the higher density case. When ionization degree is high enough, the influence of satellite lines is not important any more, and the $G+$ value converges to the G value.

The energy gap between the intercombination line and forbidden line is about 15 eV, so that electron temperature and density rarely impact the R value. When the influence of satellite line is concerned, the intensity of the peaks shifts to shorter wavelength range as the ionization degree increases. With same density, the intensity at the lower temperature is larger than in the higher temperature case.

Figure 8 shows the comparison of the experimental and theoretical R and G values. Cases A and C cooperate with the experiment very well. The difference in Case B is because of the influence of the Cu lines, which enhance the intensities of intercombination and forbidden lines and result in larger G values than Case B.

When used to diagnose the electron temperature and density of plasma, the traditional G value and R value are used separately[7]. Few of the former works discussed the influence of ionization degree on these two ratios. In Ref. [7], G value and R value are believed to be independent in some range, but they are sensitive to a parameter H-like/He-like, which is determined by electron temperature and density simultaneously. In the present work, the $G+$ and $R+$ are sensitive to both electron temperature and density in the given ranges. We think this is more reasonable in diagnosing the plasma, and the electron temperature and density should be determined by the two ratios collectively.

5. Conclusion

Two kinds of shots were performed on Shenguang II laser facility to study the spectroscopy of silicon plasmas under different plasma conditions. The spectra of two types of shots are different, which reveals that the vertical CH foil in the Type II target impacted the evolution of the plasma. X-ray spectra spanning from 6.6 Å to 6.85 Å of collisional silicon plasmas have been recorded with crystal spectrometer. With the radiative-collisional codes[23], we simulate the spectra of Shot 26 and Shot 32, and successfully reproduce most of the prominent peaks in the range of 6.6–6.85 Å. The line wavelengths between the present result and the result in Ref. [9] agree within 0.01 Å. According to the simulation results, collisional excitation produces strong He-like resonance line, and dielectronic capture produces plenty of satellite lines. The spectra of He-like ion triplet lines in 6.64–6.75 Å are strongly influenced by the satellite lines, even in He-like ion dominating conditions. The traditional G value and R value are insensitive to electron temperature and density, and they cannot be used in the diagnosing of electron temperature and density of plasma. We develop the identification of G value and R value, where the influence of the satellite lines is taken into the calculations of the line ratios. The developed line ratios, $G+$ and $R+$, are influenced by the electron temperature and density, and they can be used in plasma diagnosing in some degree.

Acknowledgements

This work was supported by the Science Challenge Project (No. TZ2016005), the National Basic Research Program of China (No. 2013CBA01503), the National Natural Science Foundation of China (Nos. 10905004, 11220101002, and 11622323), and the Fundamental Research Funds for the Central Universities.

References

1. L. Ji, N. Schulz, M. Nowak, H. L. Marshall, and T. Kallman, Astrophys. J. **700**, 977 (2009).
2. S. Watanabe, M. Sako, M. Ishida, Y. Ishisaki, S. M. Kahn, T. Kohmura, F. Nagase, F. Paerels, and T. Takahashi, Astrophys. J. **651**, 421 (2006).
3. M. A. Jimenez-Garate, C. J. Hailey, J. W. den Herder, S. Zane, and G. Ramsay, Astrophys. J. **578**, 391 (2002).
4. E. Behar and H. Netzer, Astrophys. J. **570**, 165 (2002).
5. S. Kaspi, W. N. Brandt, H. Netzer, I. M. George, G. Chartas, E. Behar, R. M. Sambruna, G. P. Garmire, and J. A. Nousek, Astrophys. J. **554**, 216 (2001).
6. A. H. Gabriel and C. Jordan, Nature **221**, 947 (1969).
7. D. Porquet and J. Dubau, Astron. Astrophys. Suppl. **143**, 495 (2000).
8. A. H. Gabriel and C. Jordan, Mon. Not. R. Astron. Soc. **145**, 241 (1969).

https://doi.org/10.1017/hpl.2018.25 Published online by Cambridge University Press

9. P. Palmeri, P. Quinet, C. Mendoza, M. A. Bautista, J. Garcia, M. C. Witthoeft, and T. R. Kallman, Astrophys. J. Suppl. **177**, 408 (2008).
10. H. G. Wei, J. R. Shi, G. Zhao, and Z. T. Liang, Astron. Astrophys. **522**, A103 (2010).
11. H. G. Wei, J. R. Shi, F. L. Wang, J. Y. Zhong, G. Y. Liang, and G. Zhao, Astron. Astrophys. **566**, A105 (2014).
12. R. D. Cowan, *Los Alamos Series in Basic and Applied Sciences* (University of California Press, Berkeley, 1981).
13. N. R. Badnell, J. Phys. B: At. Mol. Opt. Phys. **30**, 1 (1997).
14. W. Eissner, M. Jones, and H. Nussbaumer, Comput. Phys. Commun. **8**, 270 (1974).
15. M. H. Chen, K. J. Reed, D. M. McWilliams, D. S. Guo, L. Barlow, M. Lee, and V. Walker, At. Data Nucl. Data Tables **65**, 289 (1997).
16. E. Trabert and B. C. Fawcett, J. Phys. B: At. Mol. Phys. **12**, L441 (1979).
17. E. Trabert, B. C. Fawcett, and J. D. Silver, J. Phys. B: At. Mol. Phys. **15**, 3587 (1982).
18. J. P. Mosnier, R. Barchewitz, C. Senemaud, M. Cukier, and R. Dei-Cas, J. Phys. B: At. Mol. Phys. **19**, 2531 (1986).
19. A. Y. Faenov, S. A. Pikuz, and A. S. Shlyaptseva, Phys. Scr. **49**, 41 (1994).
20. N. Hell, I. Miškovičová, G. V. Brown, J. Wilms, J. Clementson, M. Hanke, P. Beiersdorfer, D. Liedahl, K. Pottschmidt, F. S. Porter, C. A. Kilbourne, R. L. Kelley, M. A. Nowak, and N. S. Schulz, Phys. Scr. T **156**, 014008 (2013).
21. D. Yuan, J. Wu, Y. Li, X. Lu, J. Zhang, C. Yin, L. Su, G. Liao, H. Wei, K. Zhang, B. Han, L. Wang, S. Jiang, K. Du, Y. Ding, J. Zhu, X. He, G. Zhao, and J. Zhang, Astrophys. J. **815**, 46 (2015).
22. Q.-L. Dong, S.-J. Wang, Q.-M. Lu, C. Huang, D. W. Yuan, X. Liu, X. X. Lin, Y. T. Li, H. G. Wei, J. Y. Zhong, J. R. Shi, S. E. Jiang, Y. K. Ding, B. B. Jiang, K. Du, X. T. He, M. Y. Yu, C. S. Liu, S. Wang, Y. J. Tang, J. Q. Zhu, G. Zhao, Z. M. Sheng, and J. Zhang, Phys. Rev. Lett. **108**, 215001 (2012).
23. B. Han, F. Wang, D. Salzmann, and G. Zhao, Publ. Astron. Soc. Jpn. **67**, 29 (2015).
24. M. F. Gu, Can. J. Phys. **86**, 675 (2008).
25. M. E. Foord, R. F. Heeter, P. A. van Hoof, R. S. Thoe, J. E. Bailey, M. E. Cuneo, H. K. Chung, D. A. Liedahl, K. B. Fournier, G. A. Chandler, V. R. Jonauskas, L. P. Mix, C. Ramsbottom, P. T. Springer, F. P. Keenan, S. J. Rose, and W. H. Goldstein, Phys. Rev. Lett. **93**, 055002 (2004).
26. M. E. Foord, R. F. Heeter, H.-K. Chung, P. A. M. van Hoof, J. E. Bailey, M. E. Cuneo, D. A. Liedahl, K. B. Fournier, V. Jonauskas, R. Kisielius, C. Ramsbottom, P. T. Springer, F. P. Keenan, S. J. Rose, and W. H. Goldstein, J. Quant. Spectrosc. Radiat. Transfer **99**, 712 (2006).
27. S. Fujioka, H. Takabe, N. Yamamoto, D. Salzmann, F. Wang, H. Nishimura, Y. Li, Q. Dong, S. Wang, Y. Zhang, Y. J. Rhee, Y. W. Lee, J. M. Han, M. Tanabe, T. Fujiwara, Y. Nakabayashi, G. Zhao, J. Zhang, and K. Mima, Nature Phys. **5**, 821 (2009).
28. B. Han, F. Wang, G. Liang, and G. Zhao, Acta Phys. Sin. **65**, 110503 (2016).
29. M. Comet, J.-C. Pain, F. Gilleron, R. Piron, D. Denis-Petit, V. Meot, G. Gosselin, P. Morel, F. Hannachi, F. Gobet, M. Tarisien, and M. Versteegen, Atomic Processes in Plasmas (APiP 2016) **1811**, 070001 (2017).
30. D. Porquet, R. Mewe, J. Dubau, A. J. J. Raassen, and J. S. Kaastra, Astron. Astrophys. **376**, 1113 (2001).
31. D. Porquet, J. Dubau, and N. Grosso, Space Sci. Rev. **157**, 103 (2010).
32. J. Sylwester, B. Sylwester, and K. J. H. Phillips, Astrophys. J. Lett. **681**, L117 (2008).
33. F. Wang, B. Han, D. Salzmann, and G. Zhao, Phys. Plasmas **24**, 041403 (2017).

https://doi.org/10.1017/hpl.2018.25 Published online by Cambridge University Press